Microstability in a "MAST-like" high confinement mode spherical tokamak equilibrium

D. J. Applegate,[a] C. M. Roach,[b] S. C. Cowley,[a] W. D. Dorland,[c] N. Joiner,[a]
R. J. Akers, N. J. Conway, A. R. Field, A. Patel, M. Valovic, and M. J. Walsh[d]
EURATOM/UKAEA Fusion Association, Culham Science Centre, Abingdon, United Kingdom

(Received 24 June 2004; accepted 4 August 2004; published online 18 October 2004)

Gyrokinetic microstability analyses, with and without electromagnetic effects, are presented for a spherical tokamak plasma equilibrium closely resembling that from a high confinement mode (H mode) discharge in the mega-ampere spherical tokamak (MAST) [A. Sykes *et al.*, Nucl. Fusion **41**, 1423 (2001)]. Electrostatic ion temperature gradient driven modes (ITG modes) were found to be unstable on all surfaces, though they are likely to be substantially stabilized by equilibrium $\mathbf{E}\times\mathbf{B}$ flow shear. Electron temperature gradient driven modes (ETG modes) have stronger growth rates that substantially exceed the equilibrium flow shearing rates. Mixing length arguments suggest that ITG modes would give rise to significant transport if they are not stabilized by sheared flows, and predict weak transport from ETG turbulence. Significant plasma flows have been neglected in this first analysis, and are probably important in the delicate balance between ITG growth rates and flow shear, and in the formation of internal transport barriers on MAST. Electromagnetic effects are found to be important even in this low β discharge, especially for longer length-scale modes with $k_\perp\rho_i < O(1)$ on the inner surfaces, where tearing parity modes are found to be the fastest growing modes, with growth rates that are sensitive to the electron collision frequency. These tearing parity microinstabilities are highly extended along the magnetic field, and have been reported in a number of spherical tokamak equilibria. [DOI: 10.1063/1.1801251]

I. MICROSTABILITY IN SPHERICAL TOKAMAK PLASMAS

Microinstabilities, with wavelengths of the order of the ion or electron Larmor radii, are widely believed to underlie anomalous transport of heat and particles in tokamaks. There is considerable interest in understanding their properties and their impact on heat and particle confinement in tokamak plasmas, including in the novel tight aspect ratio spherical tokamak (ST) plasma configuration. Heat transport coefficients have been measured by a number of STs [the Culham devices: small tight aspect ratio tokamak (Ref. 1), and mega-ampere spherical tokamak (MAST) (Refs. 2 and 3), and the Princeton national spherical tokamak experiment (NSTX) (Ref. 4)]. Ion heat transport has been found to lie close to the level predicted by neoclassical theory. The NSTX experiment has reported dominant heat transport losses occurring in the electron channel,[4,5] and the study of microinstabilities could shed important light on the underlying reasons for this interesting observation.

Plasma equilibrium and geometry crucially influence microstability through their impact on the plasma particle drift velocities. Tight aspect ratio plasmas exhibit inherently strong variation in the toroidal magnetic field, and have proved to be capable of operating at very high ratios of plasma pressure to magnetic field strength, β.[6,7] The strong magnetic field variation both increases the number of trapped particles and affects the particle drifts.[8,9] All of these factors have strong influences on microstability and some of their impacts on gyrokinetic analyses have been reported in Refs. 9–11. The stabilization of short wavelength modes could explain the striking transport barriers which have recently been observed experimentally in a number of tokamaks,[12] most recently in the Culham spherical tokamak MAST,[13] and in Ref. 11 it has been proposed that strong gradients in β may play an important role in this stabilization.

Gyrokinetic codes (which avoid many of the approximations inherent in fluid models) are now starting to be applied more routinely to the study of microstability in tokamaks, and this is largely due to recent advances in computing. Such calculations can be carried out including trapped particle and electromagnetic effects. A number of nonlinear gyrokinetic simulations, exploiting supercomputers, have studied the saturation of turbulence at length scales of the order of the ion Larmor radius [ion temperature gradient driven drift waves (ITG)] (Ref. 14) and of the order of the electron Larmor radius scale [electron temperature gradient driven drift waves (ETG)].[15] In Ref. 15 it was concluded that ETG drift waves may contribute significantly to anomalous transport in tokamaks, a possibility that had previously been widely discounted on the grounds of low mixing length estimates of their contribution to transport coefficients.

Gyrokinetic analyses of microstability for NSTX have been presented in Refs. 11 and 16, using the GS2 code.[17] It was reported there that ITG modes are stabilized and ETG modes destabilized at the high ratios of T_i/T_e which are observed in some NSTX plasmas. It has been argued that this

[a]Present address: Physics Department, Imperial College, London.
[b]Electronic mail: colin.m.roach@ukaea.org.uk
[c]Present address: Department of Physics, University of Maryland, Maryland.
[d]Present address: Walsh Scientific Ltd., Culham Science Centre, Abingdon.

could be consistent with the low levels of ion and high levels of electron heat transport in these discharges. Microstability calculations in plasma conditions which have been envisaged for a conceptual design of high β ST power plant has also been presented in Ref. 18.

In this paper we present results from the first gyrokinetic stability analysis of a MAST-like plasma which has been carried out using the GS2 code.

II. THE GS2 CODE

The GS2 code is an extended version of the initial value microstability code which is described in detail in Ref. 17, and solves, together with Maxwell's equations, the gyrokinetic equations for the perturbed distribution functions of an arbitrary number of plasma species. GS2 has been extended since the publication of Ref. 17 to include perturbations of the magnetic field in all directions (i.e., perturbations both parallel and perpendicular to the equilibrium field are included), and to become capable of fully nonlinear calculations in flux-tube geometry for arbitrary tokamak equilibria. For computational convenience, in both linear and nonlinear computations, GS2 exploits the magnetic field line following coordinates of Ref. 19, using the ballooning angle θ as the parallel coordinate. GS2 calculations have been benchmarked against a variety of microstability codes at low β and at high β in Refs. 17 and 11, respectively.

GS2 written in Fortran90 exploits parallel computers using the message passing interface, and the code is thoroughly documented and available online under an open source license given in Ref. 20. The code has been ported to a Beowulf cluster at Culham and has been interfaced to a local Culham equilibrium solver GS2D. A benchmark microstability calculation, using a local moments based equilibrium, has been repeated to verify the compilation. The equilibrium interface from GS2D to GS2 has also been thoroughly tested by successfully repeating an ideal ballooning calculation, made using the IDBAL code for a GS2D equilibrium, using the GS2D-GS2 interface.

III. MAST-LIKE CONDITIONS SELECTED FOR ANALYSIS

We have selected MAST discharge 6252, a steady plasma in the high confinement mode with edge localized modes (an ELMy H-mode plasma) and heated by neutral beam injection, as the first MAST discharge for microstability analysis with GS2. The electron temperature and density profiles have been measured using the high resolution MAST Thomson scattering system at $t \sim 265$ ms, which is well into the current flat-top (which starts around $t=150$ ms) and just before the neutral beams are switched off. Figure 1 shows a

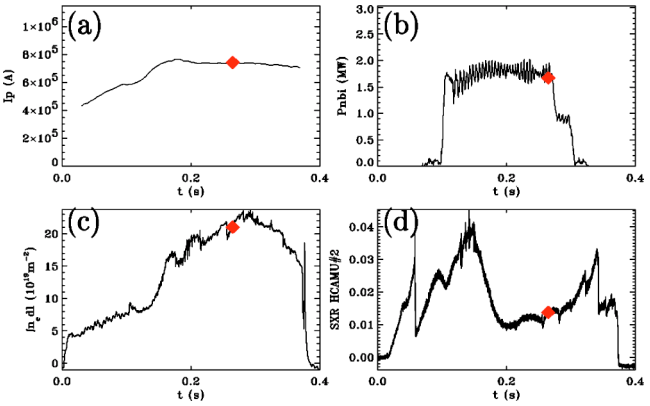

FIG. 1. (Color online). Time traces for MAST discharge 6252 of (a) plasma current, (b) neutral beam power, (c) line integrated electron density, and (d) soft x-ray intensity from a chord passing close to the plasma core. The time point where the Thomson scattering system has measured the electron temperature and density profiles is marked by the diamonds.

number of key time traces, including the intensity from a core soft x-ray channel which shows that low frequency sawteeth, have been observed in this discharge. The Thomson scattering time is well into the sawtooth ramp phase, and this is the time where we have performed microstability analyses using GS2. The EFIT equilibrium reconstruction code[21] has been used to provide an initial estimate of the equilibrium. The neutral beam injection at the timeslice of interest has been modeled using the LOCUST Monte Carlo code,[22] to provide the fast particle density and effective temperature profiles. In the calculations presented we assume that $T_i = T_e$, which is consistent with ion and electron temperature measurements, and take impurity fractions that are consistent with spectroscopy measurements. Table I shows a number of key global parameters for this MAST equilibrium.

It is well known that stability analysis is sensitive to equilibrium profiles, and it is challenging to obtain EFIT equilibrium reconstructions which adequately constrain the equilibrium pressure profile to kinetic measurements. Optimizing the match between the equilibrium pressure profile and that determined from measurements is essential, if the results of subsequent stability analyses are to relate faithfully to the experimental situation.

A. Equilibrium with consistent pressure profile

Thomson scattering gives temperature and density profile information for the electrons, and for the ions we have assumed $T_i = T_e$, estimating the ion density from a simple impurity dilution model. We model the impurities by taking a constant value of $Z_{\text{eff}} = 1.5$, and have assumed that carbon and oxygen are the only impurities and that they have den-

TABLE I. Global parameters for the MAST equilibrium at $t=0.265$ s in MAST discharge 6252, where $\overline{n_e} = (1/2a)\int n_e dl$. Across the whole plasma cross section Z_{eff} is taken to be 1.5 and impurities are assumed to be carbon and oxygen in the ratio 2:1.

B_0 (T)	I_p (MA)	R (m)	a (m)	R_{mag} (m)	$\overline{n_e}$ (m^{-3})	P_b (MW)
0.458	0.738	0.816	0.558	0.901	4.70×10^{19}	1.672

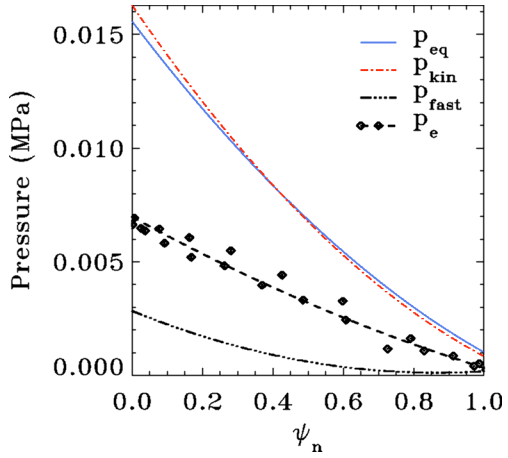

FIG. 2. (Color online). The pressure profile determined from the experimental data is plotted as a function of normalized poloidal flux ψ_n and is compared with the equilibrium pressure profile used in the GS2D equilibrium.

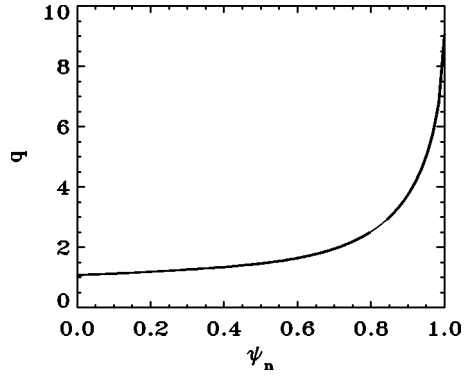

FIG. 3. Reconstructed q profile as a function of normalized poloidal flux ψ_n for MAST discharge 6252 at the Thomson scattering time.

sity profiles with the shape of the electron density profile, and with densities in the ratio 2:1. Labeling impurities with the index I and the main plasma ions with the index i, we let $c_I n/n_e$ represent the ratio of the density of impurity I to the electron density, and Z_I be the impurity atomic number. (In this case $c_C=2$, $c_O=2$, $Z_C=6$, and $Z_O=8$.) Defining additional constants $c_1=\Sigma_I Z_I^2 c_I$ and $c_2=\Sigma_I Z_I c_I$, and then combining the definition of Z_{eff} with the quasineutrality condition gives

$$\frac{n_i}{n_e}=\frac{c_1/c_2(1-Z_b n_b/n_e)-Z_{\text{eff}}+Z_b^2 n_b/n_e}{Z_i(c1/c2-Z_i)}, \tag{1}$$

$$\frac{n}{n_e}=\frac{1-Z_i n_i/n_e-Z_b n_b/n_e}{c_2}, \tag{2}$$

where n_b and Z_b represent the beam fast ion density and atomic number, respectively. The fast ion pressure p_{fast} is determined, along with the fast particle density n_b and effective temperature T_b, from Monte Carlo calculations using the LOCUST code. We take the experimentally constrained pressure profile to be given by

$$p_{\text{exp}}=T_e\left(n_e+n_i+\sum_I c_I n\right)+p_{\text{fast}}.$$

The consistency of the equilibrium reconstruction with the kinetic pressure profile has been improved using the GS2D Grad–Shafranov equilibrium solver. GS2D requires the poloidal flux on the boundary of the rectangular solution domain in R, Z, and this region is chosen to lie outside the plasma but inside the EFIT domain. We take this boundary condition from the EFIT equilibrium reconstruction. GS2D includes source terms from the poloidal field coils lying inside the solution domain and from the plasma current. The plasma current is fully specified by the toroidal field function $f(\psi)$ and the plasma pressure flux function $p(\psi)$. In GS2D the flux function $p(\psi)$ is fitted to the profile determined from the Thomson scattering measurements and the LOCUST Monte Carlo modeling of the fast ion pressure (see Fig. 2), and $f(\psi)$ is correspondingly modified so as to preserve the EFIT reconstruction of the q profile. MAST has no MSE diagnostic for measuring the q profile, but the observation of sawtooth crashes in the measurements from the central soft x-ray channel [see Fig. 1(d)] suggests that the central q is around 1, consistent with the EFIT reconstruction (Fig. 3).

Figure 4 shows the MAST equilibrium reconstruction for discharge 6252 with an equilibrium pressure profile that is consistent with experimental measurements. This equilibrium was used in the GS2 microstability calculations that are presented in this paper.

B. Surface parameters for microstability analysis

Microstability analyses have been performed on the magnetic flux surfaces $\psi_n=0.4$, 0.6, and 0.8, where ψ_n is the normalized poloidal flux. Tables II and III show the key surface parameters that were required by GS2 for local microstability analysis on each surface. Figure 5 shows how some of the profile derivatives have been estimated using the equilibrium pressure profile and Thomson scattering measurements. The normalized gradient scale length for pressure, tempera-

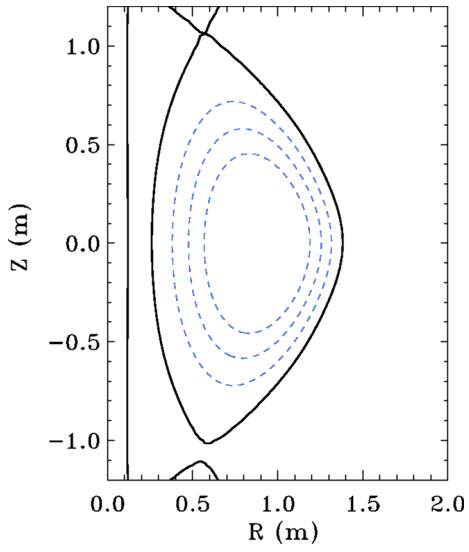

FIG. 4. (Color online). The reconstructed equilibrium separatrix (solid line) for MAST discharge 6252 at the Thomson scattering time. The dashed lines show the surfaces with normalized poloidal flux $\psi_n=0.4$, 0.6, and 0.8, where microstability analyses have been performed.

TABLE II. Surface equilibrium parameters. β is local, and defined as $\beta=4.03\times10^{-3}[n_eT_i\ (\mathrm{keV})/B_0^2]$ with n_e in $10^{19}\ \mathrm{m}^{-3}$, T_i in keV, and B_0 in T.

ψ_n	p (kPa)	a/L_p	β (%)	q	$(\psi_n/q)(dq/d\psi_n)$	a (m)	R/L_T	ρ_i (mm)
0.4	8.379	1.867	4.95	1.346	0.286	0.311	3.14	7.64
0.6	5.468	2.463	2.97	1.643	0.841	0.391	5.74	6.10
0.8	3.022	3.677	1.46	2.521	2.489	0.468	4.75	4.62

ture, or density (a/L_p, a/L_T, and a/L_n, respectively) is defined as

$$a/L_x = -\frac{1}{x(\psi_n)}\frac{dx}{d\psi_n}.$$

The collision frequencies ν (normalized as described in Sec. IV) for input into GS2 have been determined using the prescription outlined in the online GS2 documentation.[20]

The measured electron density profile is rather flat, so that a/L_{n_e} is poorly determined directly from the experimental data. The density gradient scale lengths have instead been chosen by making a simple ansatz relating the density profiles of species, and by choosing the gradients to (i) satisfy the quasineutrality condition away from the flux surface:

$$a/L_{n_e} = a/L_{n_i} + a/L_{n_b} + \sum_I a/L_{n_I}, \tag{3}$$

and (ii) be fully consistent with the assumed equilibrium pressure profile gradient:

$$a/L_p = \frac{n_iT_i}{p}(a/L_{n_i} + a/L_{T_i}) + \frac{n_eT_e}{p}(a/L_{n_e} + a/L_{T_e}) + \sum_I \frac{n_IT_I}{p}(a/L_{n_I} + a/L_{T_I}) + \frac{n_bT_b}{p}(a/L_{n_b} + a/L_{T_b}). \tag{4}$$

As in Sec. III A, we make the ansatz that the density profiles of electrons and all impurity species have the same shape. The fast ion density gradient is determined from Monte Carlo simulations. Equations (3) and (4) determine the local electron and main ion density gradients.

The resulting values for a/L_{n_e} are small and negative on the two inner surfaces, and this is not inconsistent with the experimental data from Thomson scattering.

IV. MICROSTABILITY CALCULATIONS

Here we report on the results from GS2 calculations, giving real frequencies and growth rates of the fastest growing modes as functions of the poloidal wave number k_y. In all calculations the ballooning parameter θ_0 has been set to zero.

The results are divided into two wavelength regimes: (i) poloidal wavelengths of the order of or greater than the ion Larmor radius, $k_y\rho_i \leqslant O(1)$, and (ii) poloidal wavelengths that are shorter than the ion Larmor radius, but greater than or of the order of the electron Larmor radius, $k_y\rho_e \leqslant O(1)$ and $k_y\rho_i > 1$. The first regime includes ITG, and the second includes ETG. In GS2 electromagnetic effects can be included, and it is also possible to vary the number of species which are included in the calculations. We have performed a variety of calculations to explore some of the parameters which influence microstability.

Physical quantities in GS2 are expressed in normalized units relative to a set of reference parameters which are defined as follows:

(1) Macroscopic lengths are normalized to L_{ref}, which is defined as the plasma half diameter on the equatorial mid-

TABLE III. Surface equilibrium parameters for each plasma species.

ψ_n	Species	T (keV)	a/L_T	n ($10^{19}\ \mathrm{m}^{-3}$)	a/L_n	ν
0.4	e	0.592	2.043	4.357	−0.363	0.429
0.4	D	0.592	2.043	3.982	−0.399	0.012
0.4	D beam	11.06	0.683	0.050	2.457	2.3×10^{-4}
0.4	C	0.592	2.043	0.038	−0.363	0.118
0.4	O	0.592	2.043	0.019	−0.363	0.167
0.6	e	0.377	2.797	4.097	−0.276	0.969
0.6	D	0.377	2.797	3.719	−0.301	0.028
0.6	D beam	9.38	0.869	0.029	2.949	3.4×10^{-4}
0.6	C	0.377	2.797	0.035	−0.276	0.267
0.6	O	0.377	2.797	0.018	−0.276	0.377
0.8	e	0.217	2.565	3.522	1.622	2.438
0.8	D	0.217	2.565	3.206	1.635	0.071
0.8	D beam	7.75	0.940	0.015	4.156	5.0×10^{-4}
0.8	C	0.217	2.565	0.030	1.622	0.673
0.8	O	0.217	2.565	0.015	1.622	0.950

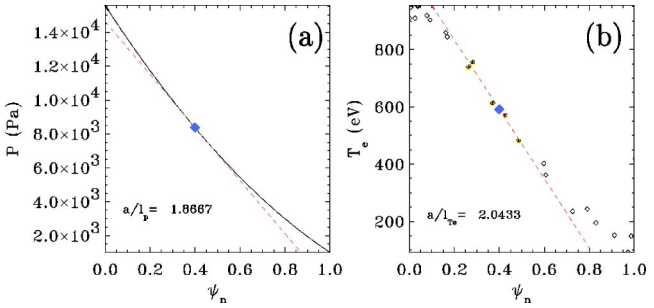

FIG. 5. (Color online). (a) Pressure and (b) electron temperature profiles from MAST 6252 at $t=0.265$ s as functions of normalized poloidal flux, and fits (dashed) to obtain their derivatives at the surface $\psi_n=0.4$.

plane. $L_{\mathrm{ref}}=0.56$ m for all surfaces in this MAST equilibrium.

(2) Masses are normalized to the deuterium mass for ITG calculations, and to the electron mass for ETG calculations.

(3) The reference temperature T_{ref} is set to the electron temperature.

(4) The reference magnetic field B_{ref} is the vacuum magnetic field on the geometric axis. $B_{\mathrm{ref}}=0.458$ T in this MAST equilibrium.

(5) The reference thermal velocity $v_t^{\mathrm{ref}}=\sqrt{T_{\mathrm{ref}}/m_{\mathrm{ref}}}$.

(6) Wave numbers are normalized to the inverse of the reference Larmor radius $\rho_{\mathrm{ref}}=m_{\mathrm{ref}}v_t^{\mathrm{ref}}/eB_{\mathrm{ref}}$.

(7) Frequencies (including collisions) are normalized to $v_t^{\mathrm{ref}}/L_{\mathrm{ref}}$.

With any numerical calculation it is important to make sure the results are well converged. The numerical accuracy of GS2 depends on grid resolutions, e.g., the numerical time step δt, and the extent and resolution of the ballooning angle θ. These grid parameters were varied to guarantee convergence of the results which are presented here. We have also checked that the results are consistent with the basic gyrokinetic ordering assumptions:

$$\rho/L \ll 1,\ \omega/\Omega \ll 1,\ \text{and}\ \gamma/\Omega \ll 1,$$

where L denotes the minimum equilibrium scale length in the system, ω is the real frequency of the instability, γ is the imaginary frequency, and Ω is the gyrofrequency. These conditions were comfortably satisfied in the calculations. The linear ballooning space calculations carried out by GS2 require the distance between mode rational surfaces to be less than the typical scalelengths of the system (L_n, L_p, and L_T). This condition is satisfied for all the calculations which are presented in this paper.

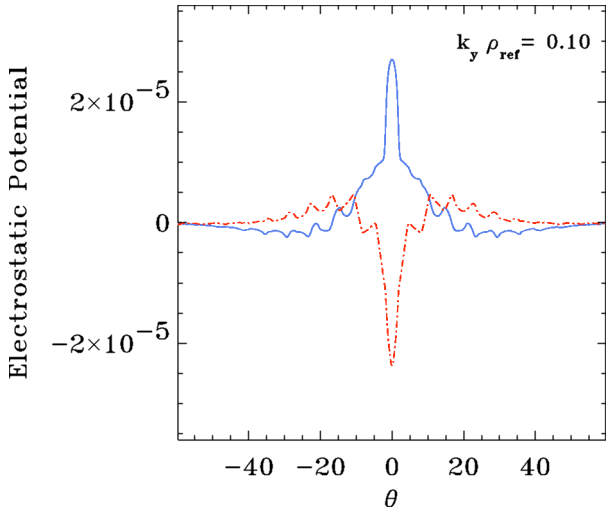

FIG. 6. (Color online). Electrostatic potential calculated by GS2 for $k_y\rho_i=0.1$ in an electrostatic ITG calculation on the surface $\psi_n=0.4$. The real part (solid line) and imaginary part (dash-dotted line) are plotted as functions of the ballooning angle θ.

A. ITG stability: $k_y\rho_i \leqslant O(1)$

The ITG calculations have been performed including all five plasma species [electrons, main ions (D), two impurity species (C and O), and beam ions (D)], both with and without electromagnetic effects. The electron physics response is calculated in full (including trapped particle dynamics), without making adiabatic approximations.

1. Magnetic surface $\psi_n=0.4$

Figure 6 shows the fastest growing eigenfunction of the electrostatic potential for $k_y\rho_i=0.1$ in an electrostatic calculation. All the electrostatic eigenfunctions on this surface are well converged in runs where the ballooning angle θ extends to $\pm 20\pi$ along the equilibrium magnetic field direction, and

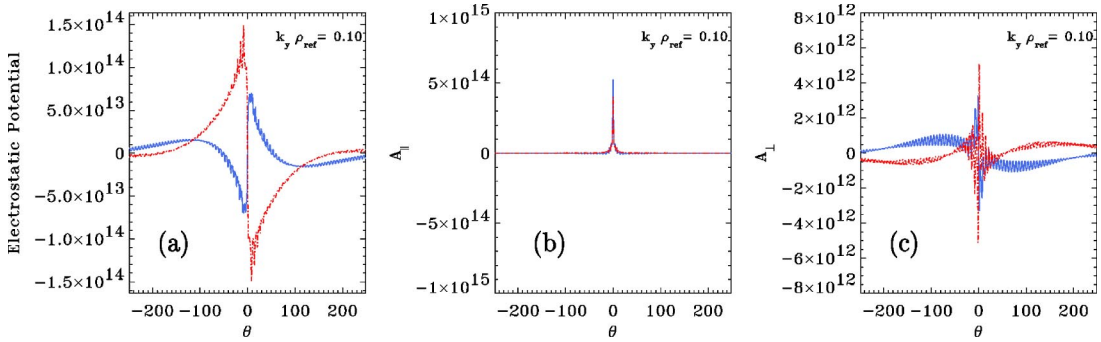

FIG. 7. (Color online). Electromagnetic eigenfunctions on the surface $\psi_n=0.4$ with $k_y\rho_i=0.1$ for (a) the electrostatic potential ϕ, (b) the parallel magnetic vector potential $A_{\parallel}$, and (c) the perpendicular magnetic vector potential $A_{\perp}$. The real and imaginary parts are represented by solid and dot-dashed lines, respectively.

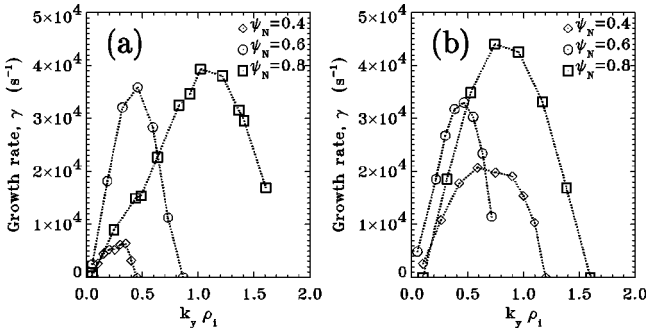

FIG. 8. ITG growth rates as a function of $k_y\rho_i$ for the $\psi_n=0.4$, 0.6, and 0.8 surfaces from (a) electrostatic calculations and (b) full electromagnetic calculations.

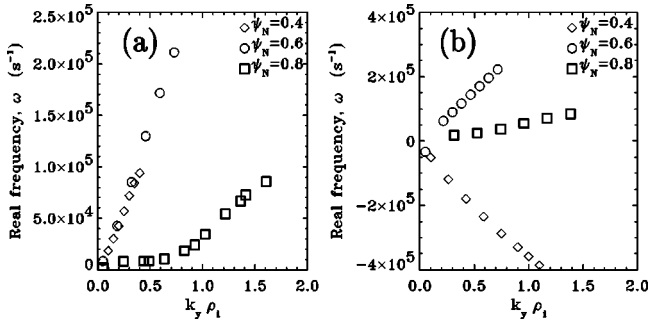

FIG. 9. ITG real frequencies as a function of $k_y\rho_i$ for the $\psi_n=0.4$, 0.6, and 0.8 surfaces from (a) electrostatic calculations and (b) full electromagnetic calculations.

are robustly reproduced when the θ grid is extended. In electromagnetic calculations the electrostatic potential eigenfunctions of the fastest growing modes were found to extend much further along the field line. The θ grid had to be extended by a factor of 4 to obtain convergence. Unfortunately, these computations are extremely expensive in computational time, as this scales with the third power with the number of points in the θ grid. Eigenfunctions for electrostatic and vector potentials are shown in Fig. 7 for electromagnetic calculations.

The ITG growth rates both for electrostatic and electromagnetic calculations are presented in Fig. 8 and the corresponding real frequencies are presented in Fig. 9. In the electrostatic calculations the real frequencies are positive and are roughly proportional to k_y (ITG modes have positive real frequencies since they propagate in the ion diamagnetic direction). The inclusion of electromagnetic effects significantly increases the growth rates of all modes in this waveband, considerably extends the potential eigenfunction along the field line, and changes the real frequencies from positive to negative. Figure 7(b) shows that the parity along the field line of the perturbed parallel magnetic potential $A_\parallel$ is even, and that the mode therefore has tearing parity. These extended electromagnetic modes are quite different from electrostatic ITG modes with electromagnetic corrections, and resemble microtearing modes.[23] Tearing modes are generally dissipative phenomena and sensitive to collisionality. Setting the collisionality to zero reduced the growth rate of the dominant instability, and the character of this mode reverted to that typical of ITG modes. (See Fig. 10 where $A_\parallel$ is odd and ϕ is even.)

The value of the gradients in ion temperature and ion density have also been altered to investigate their impact on growth rates. In particular, both electrostatic and electromagnetic modes with $k_y\rho_i=0.3$ modes were studied. In order to preserve the pressure gradient (and avoid the need to recompute the equilibrium) the temperature and density gradients were altered simultaneously. In effect the value of $\eta_i = n_i T_i'/n_i' T_i$ was modified (preserving the ion pressure gradient). The value of η_e had also to be suitably adjusted (at constant electron pressure gradient) so as to maintain quasineutrality. Figure 11 shows that in electrostatic calculations the growth rate drops dramatically as the magnitude of η_i is reduced, confirming the well-known phenomenon that at fixed pressure gradient ITG modes are more stable with steeper ion density and flatter ion temperature profiles. (ITG modes are often referred to as η_i modes.) The growth rate of the electrostatic mode as a function of η_i was observed to be symmetric about $\eta_i=0$. On the other hand, the growth rates of the electromagnetic modes are far from symmetric about $\eta_i=0$, especially in the region close to $\eta_i=0$. As η_i is reduced through zero, the growth rate of the electromagnetic mode rises sharply before reducing at higher magnitudes of η_i to reconverge with the growth rates of the electrostatic mode. Microtearing modes are known to be sensitive to η_e, and $\eta_e \sim \eta_i$ in the above scan. This study underlines the need

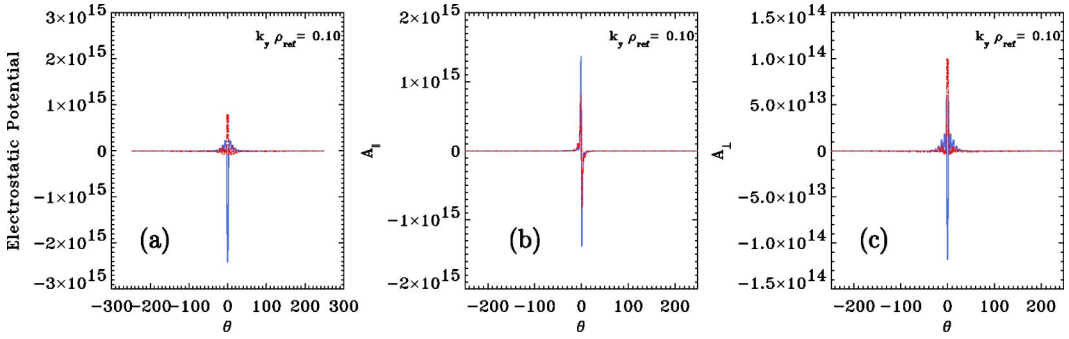

FIG. 10. (Color online). Electromagnetic collisionless GS2 eigenfunctions on the surface $\psi_n=0.4$ at $k_y\rho_i=0.1$, for (a) the electrostatic potential, (b) the parallel magnetic vector potential $A_\parallel$, and (c) the perpendicular magnetic vector potential $A_\perp$.

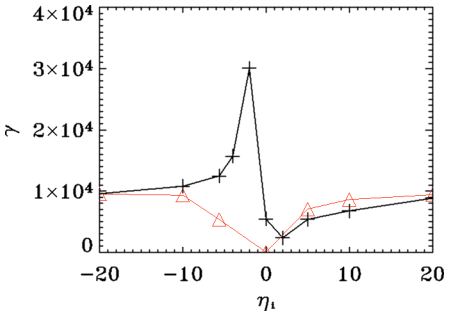

FIG. 11. (Color online). Growth rates Im(ω) as a function of η_i, for the fastest growing electrostatic and electromagnetic eigenmodes with $k_y\rho_i = 0.3$ and on the surface $\psi_n = 0.4$. The electrostatic and electromagnetic results are represented as triangles and crosses, respectively. η_i has been altered preserving the ion pressure gradient. η_e has smultaneously been modified (at constant electron pressure gradient) so as to maintain quasineutrality, resulting in $\eta_e \sim \eta_i$.

for accurate density, temperature, and pressure profiles if microstability analyses are to be relevant for experimental conditions.

These microtearing modes could be important in spherical tokamaks. Assessing their stability requires extremely large computations, owing to their highly extended nature along the equilibrium magnetic field line. A more detailed study is underway to deepen our understanding of these tearing parity instabilities.

2. Magnetic surface $\psi_n = 0.6$

The electrostatic calculations for the surface $\psi_n = 0.6$ reveal modes with the character of ITG instabilities, as can be seen from the frequency and growth rate plots in Figs. 8 and 9, and are qualitatively similar to the results from the $\psi_n = 0.4$ surface. The electromagnetic results, on the other hand, seem to show both ITG character modes and a single microtearing mode at $k_y\rho_i = 0.05$. The real frequency plot suggests the nature of each mode, and shows a discontinuous jump between $k_y\rho_i = 0.05$ and $k_y\rho_i = 0.2$. The modes at $k_y\rho_i \geqslant 0.13$ have the character of ITG modes, and the mode at $k_y\rho_i = 0.05$ has tearing parity. The $A_\parallel$ eigenfunction is even at $k_y\rho_i = 0.05$ and odd at all the other k_y values.

Overall, the effect of magnetic perturbations on growth rates for this surface is small, much smaller than for the $\psi_n = 0.4$ surface for instance. Electromagnetic results either match the electrostatic growth rates, or slightly stabilize them (particularly for higher k_y). Only the tearing mode was more unstable than the corresponding electrostatic mode, similar to observations on the $\psi_n = 0.4$ surface.

3. Magnetic surface $\psi_n = 0.8$

The electrostatic and electromagnetic results for this surface are presented in Figs. 8 and 9, which include plots of the growth rates and real frequencies as functions of $k_y\rho_i$. The dominant electromagnetic modes on this surface do not have tearing parity, and the real frequencies of the growing modes are all positive. The real frequencies are not linear in k_y, and unstable modes are found at higher values of $k_y\rho_i$ than on the inner surfaces. Electromagnetic effects are observed to destabilize the modes at low k_y and stabilize them at higher k_y.

The $\psi_n = 0.8$ magnetic surface has stronger shaping than the inner surfaces, as can be seen from Fig. 4, so that more points must be included along the field line in order to resolve the magnetic structure.

4. Surface comparison

The growth rates and real frequencies for all three magnetic surfaces are plotted together in Figs. 8 and 9, respectively. There is a clear trend of increasing growth rate with larger ψ_n, and in electrostatic calculations the maximum growth rate occurs at higher values of $k_y\rho_i$ on the outer surfaces. This latter trend is not so clear in the electromagnetic calculations, probably owing to the tearing parity modes that are predominantly found on the $\psi_n = 0.4$ surface. The values of R/L_T listed in Table II are close to 4, the critical value R/L_{Tcrit}, which was found for the onset of toroidal ITG modes in the DIII-D benchmark equilibrium of Ref. 24. The tearing parity modes dominate on the inner surface at $\psi_n = 0.4$, but these modes may remain unstable on the outer surfaces, and simply become dominated by increasingly unstable ITG modes.

B. ETG stability: $k_y\rho_i > O(1)$ and $k_y\rho_e \leqslant O(1)$

For short length scale modes, satisfying $k_y\rho_i > 1$, in linear calculations it is reasonable to model the ion physics as a single ion species (the main plasma ion) with an unmodified adiabatic response:[25]

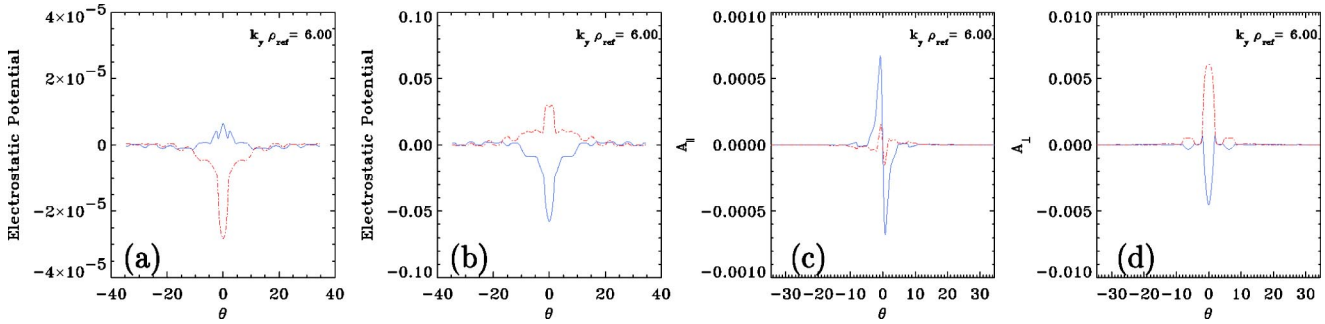

FIG. 12. (Color online). Fastest growing eigenfunctions in electrostatic and electromagnetic calculations for the flux surface $\psi_n = 0.4$ at $k_y\rho_i = 6.0$. (a) The electostatic potential for an electrostatic calculations, (b–d) show ϕ, $A_\parallel$, and $A_\perp$, respectively, for an electromagnetic calculation. The real and imaginary parts are represented by solid and dot-dashed lines, respectively.

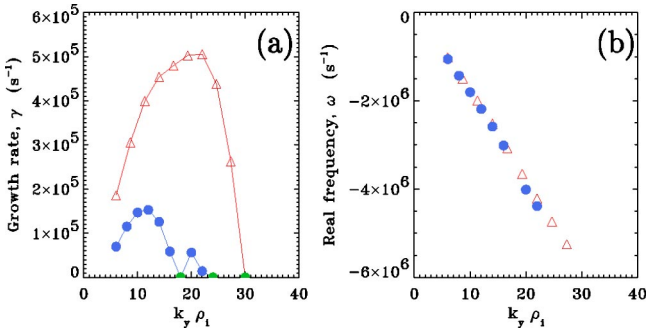

FIG. 13. (Color online). ETG (a) growth rates and (b) real frequencies of the fastest growing instabilities on the $\psi_n=0.4$ surface as functions of $k_y\rho_i$. The circles denote electromagnetic results and the triangles denote electrostatic results.

$$\frac{\tilde{n}_i}{n_i}=\frac{e\tilde{\phi}}{T_i}.$$

This approach is justified by the fact that the large ion gyroorbits effectively average over the shorter length scale turbulence. The full gyrokinetic equation need only be solved for the electrons, and this is the approach for the shorter scale instabilities studied in this section.

Figure 12 shows fastest growing eigenmodes for the electrostatic and electromagnetic calculations with $k_y\rho_i=6$ (which corresponds to $k_y\rho_e\sim 0.1$) on the $\psi_n=0.4$ flux surface. It is evident that these eigenfunctions are well contained in the θ domain simulated.

The growth rates and real frequencies for electrostatic and electromagnetic calculations on all surfaces are presented in Figs. 13–15. The growth rates are greater than those for the longer wavelength ITG and microtearing modes in the preceding section, as is typical for electron driven modes. The real frequencies are negative, and are approximately linear in k_y. Electromagnetic effects are found to have a stabilizing influence on these modes. The maximum growth rate is found at higher values of $k_y\rho_i$ as radius increases.

Two different classes of ETG instabilities were uncovered in electromagnetic calculations on the $\psi_n=0.4$ surface, and these are centered at $k_y\rho_i=12$ and $k_y\rho_i=20$, and are separated by a narrow region of stability in k_y. The transition between the two modes can also be observed as a small discontinuity in the real frequency plot at $k_y\rho_i\sim 15$.

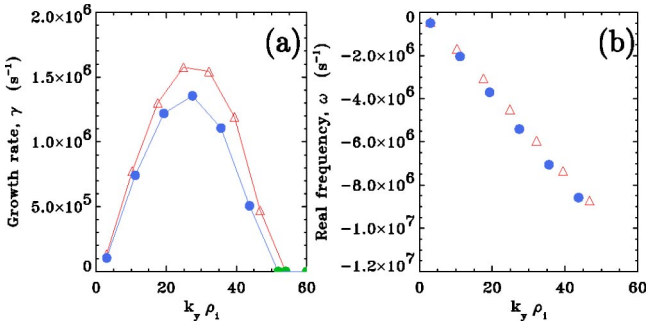

FIG. 14. (Color online). ETG (a) growth rates and (b) real frequencies of the fastest growing instabilities on the $\psi_n=0.6$ surface as functions of $k_y\rho_i$. The circles denote electromagnetic results and the triangles denote electrostatic results.

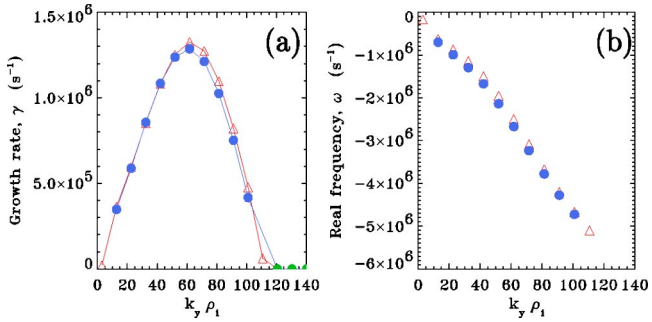

FIG. 15. (Color online). ETG (a) growth rates and (b) real frequencies of the fastest growing instabilities on the $\psi_n=0.8$ surface as functions of $k_y\rho_i$. The circles denote electromagnetic results and the triangles denote electrostatic results.

C. Mixing length estimates of transport

The equilibrium $\mathbf{E}\times\mathbf{B}$ shearing rate ω_{SE} has been estimated using an isotropic turbulence model given by Eq. (A10) in the Appendix. This is based on the Hahm–Burrell formula of Ref. 26. While toroidal rotation is included in Eq. (A10) of the Appendix, we have neglected both toroidal and poloidal rotation in all equilibrium and stability calculations and also in our numerical estimates of the shearing rate.[27] Table IV gives the estimated shearing rates along with the maximum growth rates in each wavelength regime for each surface. These estimates suggest that the shearing rate will have a moderate stabilizing effect on ITG growth rates, and virtually no effect on ETG modes at any radius due to their higher growth rates. We have made mixing length estimates of the transport coefficients which might arise from ITG and ETG turbulence using the formula

$$\chi\sim\frac{\gamma_{\max}-\omega_{SE}}{k_{\max}^2}, \tag{5}$$

where $\gamma_{\max}$ is the maximum growth rate occuring at wave number $k_{\max}$, and these are included in Table IV. Mixing length estimates suggest much higher transport from ITG modes than from ETG modes, though such estimates can be misleading. There is evidence to suggest that ETG modes are able to create very thin quasistable radial structures by coupling to one another.[15,28] These structures are known as streamers and their radial extent is much larger than the transport step length we have estimated here $(1/k_{\max})$. If these structures are present in MAST they could play an important role in electron heat transport, especially since they are unaffected by equilibrium sheared flows.

Fully nonlinear calculations are strictly necessary to predict the saturated turbulence spectrum and corresponding transport. In Ref. 15, which describes the first nonlinear simulations of ETG turbulence, it was shown that ETG modes were capable of driving a significant level of transport which is considerably in excess of mixing length estimates. Large amplitude, radially elongated, streamer structures were

TABLE IV. Table showing maximum growth rates for ETG and ITG results on different surfaces together with the corresponding ω_{SE} and χ values. All growth rates are electromagnetic and the asterisk symbol denotes a microtearing mode.

ψ_n	γ_{ITG}	γ_{ETG}	ω_{SE}	χ_{ITG}	χ_{ETG}
0.4	21000*	150000	5200	2.7	0.033
0.6	33000	1300000	6300	3.3	0.085
0.8	44000	1250000	4080	4.9	0.021

found to be very weakly damped by zonal flows, and these structures generated substantial cross field transport.

V. CONCLUSIONS

We have performed gyrokinetic microstability analyses for an equilibrium that is close to that which was obtained in the flat-top of an ELMy H-mode MAST discharge. Linear growth rates for modes with perpendicular wavelengths of the order of the ion and electron Larmor radii have been determined on three magnetic surfaces, using the GS2 code with and without full electromagnetic effects.

Electromagnetic effects have proved to be crucially important even in this relatively low β MAST discharge, especially for longer length-scale modes with wavelengths of the order of the ion Larmor radius on the inner surfaces, where tearing parity modes have been found to be the fastest growing modes. The growth rate of these modes is sensitive to the electron collision frequency, and collisions are found to enhance the instability. The modes are also highly extended along the magnetic field direction, so that even linear calculations where these instabilities are excited are extremely demanding computationally. Very similar modes have also been reported in a microstability study for a conceptual spherical tokamak power plant plasma,[18] and in studies of NSTX plasmas,[16,29] and these modes could play an important role in transporting electron heat, since electrons have extremely high parallel velocities. Nonlinear calculations of these instabilities will be extremely demanding owing to their large extent along the magnetic field line.

It has been shown that electrostatic ITG modes can be stabilized if the ion pressure gradient can be supported by the ion density profile (which was relatively flat for the equilibrium studied) instead of by the ion temperature profile. Therefore, if standard ITG modes (without tearing parity) dominate, reducing η_i by peaking the density (e.g., by pellet injection) should improve plasma performance. The dependence of the tearing parity mode growth rates on η_i (and η_e) was found to be somewhat more subtle.

It has been found that ITG modes are likely to be at least partially stabilized by shearing in the equilibrium $\mathbf{E}\times\mathbf{B}$ flow velocity. We have estimated only the diamagnetic contributions to the shearing rates, neglecting the potentially large contributions from the toroidal flows in MAST, so the ITG stabilization effect could in principle be larger. ETG modes have stronger growth rates that exceed the equilibrium $\mathbf{E}\times\mathbf{B}$ shearing rates by several orders of magnitude. Mixing length arguments suggest that the ITG modes would give rise to significant transport if they are not stabilized by sheared flows, and predict rather weak transport from ETG turbulence. Nonlinear calculations are really required to give more reliable transport coefficients. Significant plasma flows on MAST have been neglected in this first analysis, and these could be very important in determining the crucial balance between ITG growth rate and the equilibrium $\mathbf{E}\times\mathbf{B}$ velocity shearing rate, and in the formation of ITBs on MAST.

ACKNOWLEDGMENTS

The authors are grateful to Clarisse Bourdelle, Jack Connor, Jim Hastie, and Howard Wilson for useful discussions, and Peter Knight and Terry Martin for helping with a number of local system issues.

This work was funded jointly by the United Kingdom Engineering and Physical Sciences Research Council and by EURATOM.

APPENDIX: EQUILIBRIUM E×B SHEAR RATE

The $\mathbf{E}\times\mathbf{B}$ shear flow can suppress turbulent instabilities when the shearing rate ω_{SE}, given below, becomes comparable to the growth rate of the instability. Reference 26 provides the Hahm–Burrell shearing rate:

$$\omega_{SE} = \frac{\Delta\psi}{\Delta\phi}\frac{\partial^2\Phi}{\partial\psi^2}, \tag{A1}$$

where $\Phi(\psi)$ is the equilibrium electric scalar potential, ψ is the poloidal flux, and ϕ is the toroidal angle. We begin by finding $\partial^2\Phi/\partial\psi^2$, using the equilibrium equation,

$$\frac{\nabla P}{n_i e} = \mathbf{V}\times\mathbf{B} + \mathbf{E} = \mathbf{V}\times\mathbf{B} - \nabla\Phi = \mathbf{V}\times\mathbf{B} - \Phi'\,\nabla\psi, \tag{A2}$$

where primes denote differentiation with respect to ψ; $\mathbf{E}$ and P are the electric field and pressure; $\mathbf{B}$ is the magnetic field defined by $\mathbf{B}=(\nabla\psi\times\nabla\phi)+f\nabla\phi$; $\mathbf{V}$ is the ion velocity (in the toroidal direction) defined by $\mathbf{V}=\Omega(\psi)R^2\nabla\phi$, where Ω is the toroidal angular velocity and R is the major radius; and n_i and e are simply the ion number density and electronic charge magnitude. By taking the vector product of the toroidal angle gradient with the magnetic field, we obtain

$$\nabla\phi\times\mathbf{B} = \nabla\phi\times(\nabla\psi\times\nabla\phi) = \frac{\nabla\psi}{R^2}. \tag{A3}$$

Using this together with the definition for $\mathbf{V}$ we can write Eq. (A2) as

$$\frac{P'\,\nabla\psi}{n_i e} = \Omega\,\nabla\psi - \Phi'\,\nabla\psi. \tag{A4}$$

(Note that $\nabla P = P'\nabla\psi$ since P is a function of ψ only.) Hence

$$\Phi' = \Omega - \frac{1}{n_i e}P', \tag{A5}$$

$$\Phi'' = \Omega' - \frac{1}{n_i e}P'' + \frac{n_i'}{n_i^2 e}P'. \tag{A6}$$

We can use the two standard relations, $\eta_i = n_i T'/n_i' T$, and $P = n_i T$ to write n_i' as

$$n_i' = \frac{n_i P'}{P(1+\eta_i)}, \tag{A7}$$

which is substituted into Eq. (A8) to give

$$\Phi'' = \Omega' - \frac{1}{n_i e}P'' + \frac{(P')^2}{n_i e P(1+\eta_i)}. \tag{A8}$$

For isotropic turbulence where $\Delta r \sim r\Delta\theta$ it can readily be shown from the Hahm–Burrell formula [given above as equation (A1)] (see Refs. 26 and 30) that

$$\omega_{SE} = \frac{(d\psi/d\rho)^2}{B}\frac{\partial^2\Phi}{\partial\psi^2}. \tag{A9}$$

Substituting from Eq. (A8) this gives

$$\omega_{SE} = \frac{(d\psi/d\rho)^2}{B}\left(\Omega' - \frac{1}{n_i e}P'' + \frac{(P')^2}{n_i e P(1+\eta_i)}\right). \tag{A10}$$

[1] C. M. Roach, R. J. Akers, N. J. Conway, T. M. Dodge, M. P. Gryaznevich, P. Helander, A. Sykes, M. J. Walsh, S. Team, and N. Team, Nucl. Fusion **41**, 11 (2001).

[2] A. Sykes, R. J. Akers, L. C. Appel *et al.*, Nucl. Fusion **41**, 1423 (2001).

[3] R. J. Akers, J. W. Ahn, G. Y. Antar *et al.*, Plasma Phys. Controlled Fusion **45**, A175 (2003).

[4] E. J. Synakowski, M. G. Bell, R. E. Bell *et al.*, Plasma Phys. Controlled Fusion **44**, A165 (2002).

[5] This important result has yet to be confirmed by the MAST experiment. MAST has generally plasma parameters similar to NSTX, but presently has a lower level of auxiliary heating. It will be very interesting to observe whether MAST confirms the NSTX findings when its auxiliary heating power is increased.

[6] M. Gryaznevich, R. J. Akers, P. G. Carolan *et al.*, Phys. Rev. Lett. **80**, 3972 (1998).

[7] R. Maingi, M. G. Bell, R. E. Bell *et al.*, Plasma Phys. Controlled Fusion **45**, 657 (2003).

[8] C. M. Roach, J. W. Connor, and S. Janjua, Plasma Phys. Controlled Fusion **37**, 679 (1995).

[9] G. Rewoldt, W. M. Tang, S. Kaye, and J. Menard, Phys. Plasmas **3**, 1667 (1996).

[10] M. Kotschenreuther, W. Dorland, Q. P. Liu, M. C. Zarnstorff, R. L. Miller, and Y. R. Lin-Liu, Nucl. Fusion **40**, 677 (2000).

[11] C. Bourdelle, W. Dorland, X. Garbet, G. W. Hammett, M. Kotschenreuther, G. Rewoldt, and E. J. Synakowski, Phys. Plasmas **10**, 2881 (2003).

[12] P. Gohil, J. Kinsey, V. Parail *et al.*, Nucl. Fusion **43**, 708 (2003).

[13] H. Meyer, A. R. Field, R. J. Akers *et al.*, Plasma Phys. Controlled Fusion **46**, A291 (2004).

[14] J. Candy and R. E. Waltz, Phys. Rev. Lett. **91**, 045001 (2003).

[15] W. Dorland, F. Jenko, M. Kotschenreuther, and B. N. Rogers, Phys. Rev. Lett. **85**, 5579 (2000).

[16] M. H. Redi, W. Dorland, R. Bell *et al.*, in *Proceedings of 30th EPS Conference on Controlled Fusion and Plasma Physics, St. Petersburg*, edited by R. Koch and S. Lebedev (European Physical Society, Mulhouse, 2003), ECA Vol. 27A, p. 4.94.

[17] M. Kotschenreuther, G. Rewoldt, and W. M. Tang, Comput. Phys. Commun. **88**, 128 (1995).

[18] H. R. Wilson, J. W. Ahn, R. J. Akers *et al.*, Nucl. Fusion **44**, 917 (2004).

[19] M. A. Beer, S. C. Cowley, and G. W. Hammett, Phys. Plasmas **2**, 2687 (1995).

[20] See http://gs2.sourceforge.gs2.net

[21] L. L. Lao, H. S. John, R. D. Stambaugh *et al.*, Nucl. Fusion **25**, 1611 (1985).

[22] R. J. Akers, L. C. Appel, P. G. Carolan *et al.*, Nucl. Fusion **42**, 122 (2002).

[23] Similar modes have also been found in the conditions of the NSTX experiment (Refs. 16 and 29), and in the study of a conceptual ST power plant (Ref. 18). These modes could be important in spherical tokamaks.

[24] A. M. Dimits, G. Bateman, M. A. Beer *et al.*, Phys. Plasmas **7**, 969 (2000).

[25] As the ion orbits are larger than the turbulence wavelengths, the ions respond to the full perturbed potential and not just the flux surface varying part as in the case of the electron response to ITG turbulence.

[26] T. Hahm and K. Burrell, Phys. Plasmas **2**, 1648 (1995).

[27] It should however be pointed out that toroidal rotation can be significant in MAST beam heated discharges. The equilibrium $\mathbf{E}\times\mathbf{B}$ shearing rate is notorioulsy difficult to estimate accurately, and here we are only seeking to compare its approximate magnitude with the mode growth rates.

[28] F. Jenko, W. Dorland, M. Kotschenreuther, and B. N. Rogers, Phys. Plasmas **7**, 1904 (2000).

[29] C. Bourdelle (private communication).

[30] J. W. Connor and H. R. Wilson, Plasma Phys. Controlled Fusion **42**, R1 (2000).